Antichirality Emergent in Type-II Weyl Phononic Crystals

Mou Yan,[1,5] Xueqin Huang,[2] Jien Wu,[2] Weiyin Deng,[3,*] Jiuyang Lu,[3,†] and Zhengyou Liu[3,4,‡]
[1]School of Physics and Microelectronics, Key Laboratory of Materials Physics of Ministry of Education, Zhengzhou University, Zhengzhou 450001, China
[2]School of Physics and Optoelectronics, South China University of Technology, Guangzhou 510640, China
[3]Key Laboratory of Artificial Micro- and Nanostructures of Ministry of Education and School of Physics and Technology, Wuhan University, Wuhan 430072, China
[4]Institute for Advanced Studies, Wuhan University, Wuhan 430072, China
[5]Institute of Quantum Materials and Physics, Henan Academy of Sciences, Zhengzhou 450046, China

(Received 23 November 2022; accepted 6 June 2023; published 30 June 2023)

Chiral anomaly as the hallmark feature lies in the heart of the researches for Weyl semimetal. It is rooted in the zeroth Landau level of the system with an applied magnetic field. Chirality or antichirality characterizes the propagation property of the one-way zeroth Landau level mode, and antichirality means an opposite group velocity compared to the case of chirality. Chirality is commonly observed for Weyl semimetals. Interestingly, the type-II Weyl point, with the overtilted dispersion, may flip the chirality to the antichirality, which, however, is yet to be evidenced despite numerous previous experimental efforts. Here, we implement the type-II Weyl point in sonic crystals, and by creating the pseudomagnetic fields with geometric deformation, the chirality flip of zeroth Landau levels is unambiguously demonstrated. Our Letter unveils the novel antichiral transport in the presence of time-reversal symmetry, and paves the way toward the state-of-the-art manipulation of sound waves.

DOI: 10.1103/PhysRevLett.130.266304

The discovery of topological semimetals builds a new bridge between particle physics and condensed-matter physics [1,2]. A typical example is Weyl semimetal, which possesses twofold linear crossing points in three-dimensional (3D) momentum space known as Weyl points (WPs) [3]. The low excitation around the WP is described by the Weyl equation, and thus behaves as the Weyl quasiparticle, similar to the relativistic spin-1/2 fermion in quantum field theory [4]. The WP carries topological charge $+1$ or -1, supporting the Fermi-arc dispersion on the surface [5–7] and the chiral zeroth Landau level (LL) under a strong magnetic field [8,9]. Unlike the other LLs with parabolic dispersions, the zeroth one is the linear dispersion near the WP along the direction of the magnetic field, whose slope (group velocity) is related with the topological charge of WP [9]. While adding an electric field parallel to the magnetic field, the Weyl quasiparticle is pumped between the WPs with opposite charges through the zeroth LL, giving rise to nonconservation of chiral currents, i.e., chiral anomaly [10,11]. Both the chiral zeroth LL [12,13] and the negative magnetoresistance induced by chiral anomaly [14–16] have recently been observed in experiments.

Without the limitation of the Lorentz symmetry, the excitations in topological semimetals have new physical phenomena, such as the type-II WP [17] and spin-1 WP [18], beyond the analogs of particle physics. The type-II WP has an overtilted dispersion (Fig. 1) and possesses a conical Fermi surface, different from the normal WP, as the type-I WP, with a pointlike Fermi surface [17]. The overtilted feature of type-II WP may flip the direction of group velocity of the zeroth LL near the WP, while the charge of the associated WP is not changed [19–21]. It is called that as the antichiral zeroth LL, which displays an S-like shaped dispersion in a larger wave vector range [20]. Until now, it is not clear whether the antichiral property of

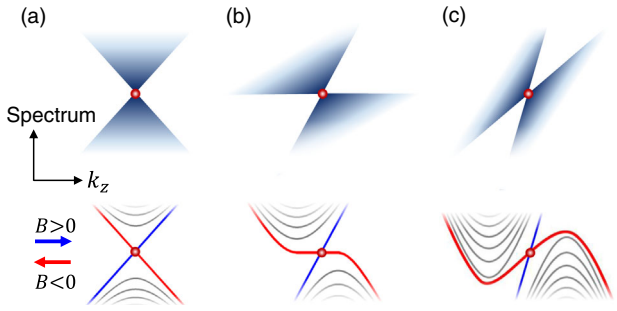

FIG. 1. (a) Chiral zeroth LLs (lower panel) for the type-I WP (upper panel). The red dot represents the positive charged WP. The red (blue) curve denotes the zeroth LL with the magnetic field antiparallel (parallel) to the wave vector k_z, and the gray curves denoted the other LLs. (b) Critical zeroth LLs for the critical WP. One of the LLs (red curve) has zero group velocity near the WP. (c) Antichiral zeroth LLs for the type-II WP. The antichiral LL (red curve) possesses an S-like shaped dispersion in a wide wave vector range. Because of the overtilted dispersion of type-II WP, the group velocity of the LL (red curve) near the WP flips from negative to positive, although topological charge of WP and the direction of the magnetic field are unchanged.

 © 2023 American Physical Society

the zeroth LL can generate reliable measurable signals in transport experiments [21]. Meanwhile, the antichiral LL, originating from the overtilted dispersion of WP, is challenging to be distinguished from other LLs in the spectrum measurement [22]. Therefore, although numerous experimental efforts on type-II Weyl physics [23–30], the antichiral LL has not been demonstrated in reality.

Sonic crystals (SCs), benefited from the macroscopic scale that can be designed and tuned freely, have recently become an ideal platform for studying abundant topological physics [31–36]. Specifically, the type-I Weyl SCs with pseudomagnetic field (PMF) have been experimentally observed [33,34]. In this Letter, we realize a PMF in a type-II Weyl SC, and evidently observe the antichiral zeroth LL. Different from the real magnetic field, the PMF is generated by a gradient structure change in space, and thus does not break the time-reversal symmetry [37]. We accurately construct the gradient deformed scatterers in an ideal type-II Weyl SC, and achieve a uniform PMF along the tilt direction of the WP. We then observe the dispersions of the antichiral zeroth LLs, together with the sublattice polarization in such a gradient type-II Weyl SC. Both the theoretical calculations and experimental observations consistently verify the antichiral zeroth LLs.

To illustrate the mechanism of the antichiral zeroth LLs, we start from an effective Hamiltonian of the WP, which is tilted along the z direction and given by [36]

$$\delta H_0 = v_0 \delta k_z + v_x \delta k_x \sigma_x + v_y \delta k_y \sigma_y + v_z \delta k_z \sigma_z, \quad (1)$$

where $\delta \boldsymbol{k}$ is the momentum deviation from the WP, $\boldsymbol{\sigma}$ are the Pauli matrices, $v_{x,y,z}$ and v_0 are the quantities related to the group velocities. The WP is type I for $|v_0/v_z| < 1$, critical for $|v_0/v_z| = 1$, and type-II for $|v_0/v_z| > 1$. The topological charge of the WP is $\chi = \mathrm{sgn}(v_x v_y v_z)$. When considering a magnetic field along the z direction with $\boldsymbol{B} = (0, 0, B)$, the Hamiltonian can be written to

$$\delta H = v_0 \delta k_z + v_x (\delta k_x + By) \sigma_x + v_y \delta k_y \sigma_y + v_z \delta k_z \sigma_z, \quad (2)$$

in which the electron charge is taken to be 1. The zeroth LL spectrum is derived as

$$\varepsilon_{LL0} = v_0 \delta k_z + \chi |v_z| \mathrm{sgn}(B) \delta k_z, \quad (3)$$

and its group velocity is obtained by $v_{LL0} = \partial \varepsilon_{LL0} / \partial \delta k_z = v_0 + \chi |v_z| \mathrm{sgn}(B)$. The latter term of the group velocity can be defined as $v_{LLz} = \chi |v_z| \mathrm{sgn}(B)$, which indicates that the zeroth LL is chiral without the tilted effect. When v_{LL0} and v_{LLz} have different signs, the zeroth LL is antichiral, owning to the v_0 term originating from the overtilted dispersion. So the group velocity is the evidence of the chiral or antichiral zeroth Landau levels. The eigenvector of the zeroth LL is polarized with the form $\psi_{LL0} = (\varphi, 0)^T$ for $\mathrm{sgn}(v_x v_y B) = 1$ and $(0, \varphi)^T$ for $\mathrm{sgn}(v_x v_y B) = -1$, where φ is the normalized wave function.

As a concrete example, Fig. 1 shows the projected bulk spectra (upper panels) and corresponding LLs (lower panels) for the WPs with positive charge $\chi = 1$ (red dot). The parameters are chosen to $v_0 = 0$ for the type-I WP [Fig. 1(a)], $v_0 = v_z$ for the critical WP [Fig. 1(b)], $v_0 > v_z$ for the type-II WP [Fig. 1(c)], and $v_z > 0$ in all three cases. The zeroth LLs (red and blue curves) are satisfied by the ε_{LL0} expression of Eq. (3). When the magnetic field is along the positive direction, $v_{LLz} = v_z$ and $v_{LL0} = v_0 + v_z > 0$ (blue curves). Since v_{LLz} and v_{LL0} have the same signs, the zeroth LLs for all the three types of WPs are chiral. For the magnetic field along the negative direction, $v_{LLz} = -v_z$ and $v_{LL0} = v_0 - v_z$ (red curves). In this case, the velocity of the zeroth LL is negative for the type-I WP, zeroth for the critical WP, but positive for the type-II WP. Therefore, v_{LL0} and v_{LLz} have different signs for the type-II WP. The overtilted dispersion of type-II WP flips the direction of group velocity of the zeroth LL near the WP from negative to positive, which means the zeroth LL turns from chirality to antichirality. This so-called antichiral zeroth LL displays an S-like shaped dispersion in a larger wave vector range.

The antichiral zeroth LL for the type-II WP can be realized in the Weyl SCs with PMF constructed by the gradient deformed scatterers. The SC is a layer-stacked 3D structure with the unit cell shown in Fig. 2(a). The lattice constant in the x-y plane is $a = \sqrt{3}$ cm and along the z direction is $h = 0.5a$. A triangular scatterer with side length $l_0 = 0.606a$ locates at the center of each unit cell and is sandwiched between plates with a thickness of $0.1a$. The unit cell in each layer forms a honeycomb lattice with two inequivalent sublattices labeled as A and B. The scatterer's side along the y direction is adjustable, by a parameter η, and is originally equal to the other two sides. Specifically, $\eta > 1.0$ and $\eta < 1.0$ correspond to the stretching and compression of the triangular scatterers, respectively. The interlayer couplings are introduced by two holes penetrated in the plate with radii $r_a = 0.1a$ and $r_b = 0.2a$.

Within this structure of $\eta = 1.0$, the first and the second bands touch at specific WPs distributing in the first Brillouin zone, denoted by the dots K/H and K'/H' in Fig. 2(b). Taking WP at the K point with coordinates $(-4\pi/3a, 0, 0.128\pi/h)$ as an example, it is a type-II WP featured by the tilted dispersions along the k_z direction as shown in the left panel of Fig. 2(c). Based on a $k \cdot p$ perturbation theory, the WP can be characterized by an effective Hamiltonian (see Supplemental Material, Sec. I [38]) as given in Eq. (1), where the Pauli matrices represent sublattice (A and B) degree of freedom, and the parameters v_0, and $v_{x,y,z}$ can be obtained by calculating inner products of an operator $\boldsymbol{p} = -i(2\rho^{-1}\nabla + \nabla\rho^{-1})$ (where ρ is the density of air and ∇ denotes the gradient operator). In a basis of the two states, with their simulated pressure field distributions

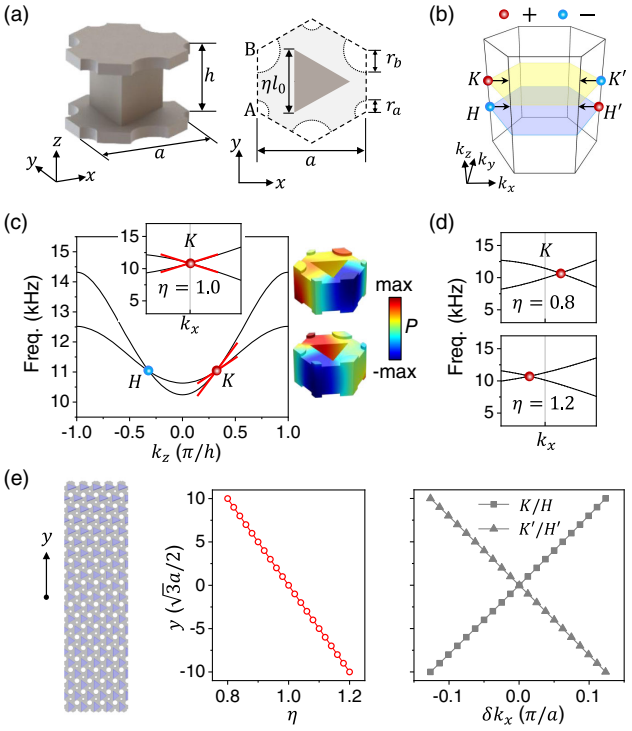

FIG. 2. (a) Side (left panel) and top (right panel) views of the unit cell, where η is the adjustable parameter to introducing deformation. (b) First Brillouin zone. The dots in red (blue) colors represent the WPs with topological charges $+1$ (-1). The arrows indicate the shift direction of the WPs. (c) Left panel: Bulk band structures along the k_z direction at $(k_x, k_y) = (-4\pi/3a, 0)$ and along the k_x directions (inset) near the K point. The red lines are the band structures predicted by corresponding effective Hamiltonians. Right panel: Pressure field distributions of two degenerate Bloch states. (d) WP shifts along the k_x direction for $\eta = 0.8$ and 1.2. (e) Left and middle panels: Realization of PMF with gradient structure which is implemented through the variation of η along the y direction (red circles). Right panel: Location shifts with respect to y for WPs near the K/H and K'/H' points (squares and triangles).

shown in the right panel of Fig. 2(c), the nonzero independent components of $\boldsymbol{p}$ are $p_{z,11} = 0.14cf_W$, $p_{z,22} = 0.28cf_W$, and $p_{x,12} = (0.59 - i0.87)cf_W$. Taking the frequency of WP $f_W = 11.03$ kHz and the sound velocity $c = 343$ m/s, the parameters are estimated as $v_0 = (p_{z,11} + p_{z,22})/2f_W = 0.21c$, $v_x = |p_{x,12}|/2f_W = 0.53c$, $v_y = -v_x$ and $v_z = (p_{z,11} - p_{z,22})/2f_W = -0.07c$. The effectiveness of the Hamiltonian can be verified by comparing the simulated and derived bulk dispersions around the K point, which are denoted by black curves and red lines in Fig. 2(c), respectively. The derived slopes of the red lines are $\pm v_x \approx \pm 0.53c$ along the x direction, and $v_0 \pm v_z \approx 0.14c$ and $0.28c$ along the z direction, which agree well with the simulated results.

The WP at the K point can be demonstrated, from its effective Hamiltonian, to carry a topological charge $\chi = -\mathrm{sgn}(v_z) = +1$ for the first band. The charges of the other three type-II WPs can be determined by the crystalline symmetries of the SC. The WPs at K and H' are related by time-reversal symmetry and have the same charge $+1$, while the WPs at K' and H are the mirror images of the above ones and have opposite charge -1. Protected by these symmetries, the SC is an ideal type-II WP system, where all the WPs emerge at the same frequency of 11.02 kHz. When η deviates from 1.0, the type-II WPs will not disappear but moving along the k_x direction and carry the same charges. For WP originally at the K point, as shown in the right panel of Fig. 2(d), its location shifts forward and backward for the cases of $\eta = 1.2$ and $\eta = 0.8$, respectively. The location shifts for the other three WPs are illustrated in Fig. 2(b), where the arrows denote shift directions as η increseas.

The key to generating artificial PMF is to construct a gradient Weyl SC with a nonuniform pseudovector potential $\boldsymbol{A}(x, y, z)$. The pseudovector potential enters the effective Hamiltonian by taking the replacement $\delta\boldsymbol{k} \to \delta\boldsymbol{k} - \boldsymbol{A}$. In our design, since the parameter η can shift the WP along the k_x direction, the pseudovector potential can be realized by forcing specific movement of the WPs for different part of the SC. A practice scheme is to adopt the Landau gauge and elaborate the structure with gradually deformed scatterers arranged along the y direction. By linearly tuning η along the y direction (from 0.8 to 1.2), as illustrated by the red circles in Fig. 2(e), the WPs show good linear shifts with respect to their original positions. In this way, the pseudovector potential reads $\boldsymbol{A} = (-By, 0, 0)$ and an artificial PMF is established. The PMF is proportional to the structural deformation according to $\boldsymbol{B} = \nabla \times \boldsymbol{A}$. For the WP near the K point, the magnitude of the PMF is $0.047/a\hat{2}$. Meanwhile, the WP near the H point is subject to the same PMF, while for the WPs near the K' and H' points, the synthetic PMFs are of the same magnitude but opposite direction.

Under the PMF, the energy spectra around the WPs split into a series of discrete LLs. In type-II Weyl systems, since the group velocities are overflipped, the associated zeroth LLs have characteristic antichiral properties and a specific S-like profile. For the WP near the K point, the PMF is oriented to the $-z$ direction, i.e., $B = -0.047a^{-2} < 0$, the effective Hamiltonian is described by Eq. (2), and the spectrum of the zeroth LL given by Eq. (3) is $\varepsilon_{LL0} = (v_0 + v_z)\delta k_z$ with group velocity $v_{LL0} = v_0 + v_z = 0.14c$ and $v_{LLz} = v_z = -0.07c$. Therefore, the overtilted term v_0 flips the group velocity from negative ($v_{LLz} < 0$) to positive ($v_{LL0} > 0$), turning the chiral zeroth LL to the antichiral one. The zeroth LLs for the H, K', and H' points have the negative, positive, and negative group velocities, respectively. They are antichiral as well, since their velocities v_{LL0} and v_{LLz} have different signs, as discussed in Supplemental Material, Sec. I [38]. This feature is unique for the PMF without breaking the time-reversal symmetry of the system, in which the PMFs for the K and H points

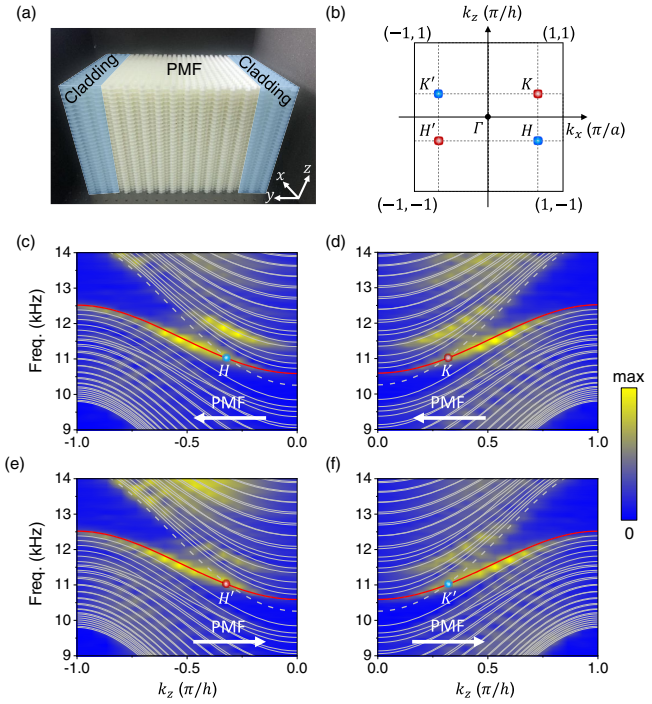

FIG. 3. (a) Photo of the sample. The white region represents the gradient type-II Weyl phononic crystal, and the light blue regions denote the cladding structures. (b) Projected surface Brillouin zone in the k_x-k_z plane. (c), (d), (e), and (f) projected dispersions of the LLs near the WPs K, H, K', and H'. The colored maps denote the magnitudes of experimental Fourier spectra and the lines are the simulated results. The white arrows denote the directions of the PMFs.

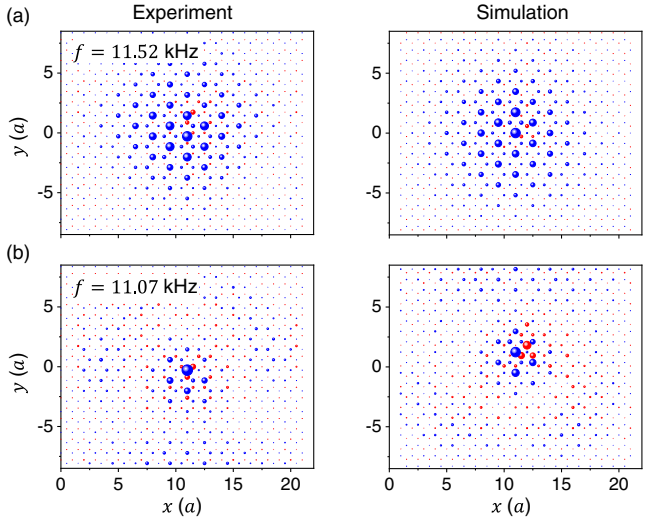

FIG. 4. (a) and (b) Measure (left panel) and simulated (right panel) acoustic intensity distributions at the frequencies of 11.52 and 11.07 kHz (with $k_z = 0.5\pi/h$) corresponding to zeroth and the other LL, respectively. Blue (red) spheres denote the positions of A (B) sublattice and the sizes represent the normalized intensity of the acoustic field.

have the opposite direction to the ones for the K' and H' points.

In experiment, we fabricate the sample through 3D printing, as shown in Fig. 3(a). The sample contains the gradient type-II Weyl SC (white region) and the cladding structures (light blue region). It has 31 layers along the z direction and 20×21 unit cells in the x-y plane. The gradient deformation of the scatterers is along the y direction and induces the PMFs along the z direction. To avoid the coupling of the surface states and the bulk states of zeroth LLs in the finite stripe, the cladding structures are added on both ends of the gradient structure, giving rise to boundary potentials to remove the Fermi-arc surface states (see Supplemental Material, Sec. II [38]). We can obtain the projected dispersion with LLs as functions of k_x and k_z. The projected surface Brillouin zone is depicted in Fig. 3(b), where K, K', H, and H' are the positions of the projected WPs with topological charge $+1$ (red dot) and -1 (blue dot).

To show the zeroth LL directly, we plot the projected dispersion as a function of k_z for a fixed k_x crossing the projected WP. Figure 3(c) shows the LLs crossing the projected WP H with topological charge -1 for $k_x = 2\pi/3a$. The red line is the calculated zeroth LL, while the white lines are the other LLs. The group velocity of the zeroth LL v_{LL0} is negative in the presence of the charge -1 of WP and the $-z$ direction of PMF, while v_{LL0} is positive in the type-I Weyl system since $v_0 = 0$, thus the zeroth LL is antichiral as predicted. In experiment, we put the source on the top center of the sample, and acquire the 3D acoustic pressure fields through the automatic scanning platform with small probe (diameter less than 3 mm). The colored maps denote the measured results, in which the antichiral zeroth LL is well consistent with the simulated one. Similarly, the simulated and measured results of the antichiral zeroth LL near the projected WP K are shown in Fig. 3(d), in which the source is put on the bottom center of the sample in experiment due to the positive group velocity of the zeroth LL. The zeroth LLs for the projected WPs K' and H' are also demonstrated, as shown in Figs. 3(e) and 3(f), respectively. In addition, we can flip the directions of the PMFs by reversing the deformation of the scatterers, producing the chiral zeroth LLs for all the WPs simultaneously (see Supplemental Material, Sec. II [38]).

Owning to $\mathrm{sgn}(v_x v_y B) = 1$ for all the four WPs, the eigenvectors of the zeroth LLs are all polarized at the A sublattice of the SC. To demonstrate the pressure field distributions of the LLs, we utilize a point source to excite the bulk states, measure the 3D field distributions in the sample, and then Fourier transform the associated field distributions in the z direction (see Supplemental Material, Sec. III [38]). The point source is set at the center of the bottom surface of the sample to stimulate the bulk states with positive k_z component. At the frequency of 11.52 kHz, the measured pressure field intensity of the zeroth LL is shown in Fig. 4(a) (left panel) for $k_z = 0.5\pi/h$, and the corresponding simulated result is shown in the right panel.

The blue and red spheres denote the positions of A and B sublattices, and their sizes represent the pressure field intensities. It is seen that both the measured and simulated results exhibit the exponential decay of the pressure fields away from the bulk center. More importantly, they mainly localize at the A sublattice, showing the property of the sublattice polarization for a fixed k_z. It is noted that the sublattice polarization effect exists for all k_z in the zeroth LL. As a contrast, we simulate and measure the field distributions of the other LL at the frequency of 11.07 kHz, as illustrated in Fig. 4(b), which distributes uniformly on both the A and B sublattices and diffuses in the whole x-y plane.

In conclusion, we have directly observed the antichiral zeroth LLs with sublattice polarization in a gradient type-II Weyl SC, where the uniform acoustic PMF is achieved through constructing the gradient deformed scatterers. Our results are also well consistent with a tight-binding model, as discussed in Supplemental Material, Sec. IV [38]. The flexible design of PMF in our system provides a special advantage to explore the LL physics of Weyl semimetals under the magnetic field, including the LL spectrum collapses [39] and 3D quantum Hall effect [40,41]. In addition, the antichiral zeroth LLs can give rise to unidirectional propagation of bulk acoustic waves, enriching the manipulation of acoustic waves.

This work is supported by the National Key R&D Program of China (No. 2022YFA1404500, No. 2022YFA1404900, No. 2018YFA0305800), National Natural Science Foundation of China (No. 11890701, No. 11974120, No. 11974005, No. 12074128, No. 12222405, No. 12204290), Guangdong Basic and Applied Basic Research Foundation (No. 2019B151502012, No. 2021B1515020086, No. 2022B1515020102, No. 2021A1515110812), and Cross-disciplinary Innovative Research Group Project of Henan Province (Grant No. 232300421004).

*Corresponding author.
dengwy@whu.edu.cn
†Corresponding author.
jylu@whu.edu.cn
‡Corresponding author.
zyliu@whu.edu.cn

[1] A. A. Burkov, Topological semimetals, Nat. Mater. **15**, 1145 (2016).
[2] N. P. Armitage, E. J. Mele, and A. Vishwanath, Weyl and Dirac semimetals in three-dimensional solids, Rev. Mod. Phys. **90**, 015001 (2018).
[3] X. Wan, A. M. Turner, A. Vishwanath, and S. Y. Savrasov, Topological semimetal and Fermi-arc surface states in the electronic structure of pyrochlore iridates, Phys. Rev. B **83**, 205101 (2011).
[4] B. A. Bernevig, It's been a Weyl coming, Nat. Phys. **11**, 698 (2015).
[5] H. Weng, C. Fang, Z. Fang, B. A. Bernevig, and X. Dai, Weyl Semimetal Phase in Noncentrosymmetric Transition-Metal Monophosphides, Phys. Rev. X **5**, 011029 (2015).
[6] S. Y. Xu, I. Belopolski, N. Alidoust, M. Neupane, G. Bian, C. Zhang, R. Sankar, G. Chang, Z. Yuan, and C. C. Lee, Discovery of a Weyl fermion semimetal and topological Fermi arcs, Science **349**, 613 (2015).
[7] B. Q. Lv, H. M. Weng, B. B. Fu, X. P. Wang, H. Miao, J. Ma, P. Richard, X. C. Huang, L. X. Zhao, G. F. Chen, Z. Fang, X. Dai, T. Qian, and H. Ding, Experimental Discovery of Weyl Semimetal TaAs, Phys. Rev. X **5**, 031013 (2015).
[8] A. A. Zyuzin and A. A. Burkov, Topological response in Weyl semimetals and the chiral anomaly, Phys. Rev. B **86**, 115133 (2012).
[9] M. X. Deng, G. Y. Qi, R. Ma, R. Shen, R. Q. Wang, L. Sheng, and D. Y. Xing, Quantum Oscillations of the Positive Longitudinal Magnetoconductivity: A Fingerprint for Identifying Weyl Semimetals, Phys. Rev. Lett. **122**, 036601 (2019).
[10] D. T. Son and B. Z. Spivak, Chiral anomaly and classical negative magnetoresistance of Weyl metals, Phys. Rev. B **88**, 104412 (2013).
[11] A. A. Burkov, Negative longitudinal magnetoresistance in Dirac and Weyl metals, Phys. Rev. B **91**, 245157 (2015).
[12] X. Yuan *et al.*, Chiral Landau levels in Weyl semimetal NbAs with multiple topological carriers, Nat. Commun. **9**, 1854 (2018).
[13] H. Jia, R. Zhang, W. Gao, Q. Guo, B. Yang, J. Hu, Y. Bi, Y. Xiang, C. Liu, and S. Zhang, Observation of chiral zero mode in inhomogeneous three-dimensional Weyl metamaterials, Science **363**, 148 (2019).
[14] X. Huang, L. Zhao, Y. Long, P. Wang, D. Chen, Z. Yang, H. Liang, M. Xue, H. Weng, Z. Fang, X. Dai, and G. Chen, Observation of the Chiral-Anomaly-Induced Negative Magnetoresistance in 3D Weyl Semimetal TaAs, Phys. Rev. X **5**, 031023 (2015).
[15] C. L. Zhang *et al.*, Signatures of the Adler-Bell-Jackiw chiral anomaly in a Weyl fermion semimetal, Nat. Commun. **7**, 10735 (2016).
[16] N. P. Ong and S. Liang, Experimental signatures of the chiral anomaly in Dirac-Weyl semimetals, Nat. Rev. Phys. **3**, 394 (2021).
[17] A. A. Soluyanov, D. Gresch, Z. Wang, Q. Wu, M. Troyer, X. Dai, and B. A. Bernevig, Type-II Weyl semimetals, Nature (London) **527**, 495 (2015).
[18] B. Bradlyn, J. Cano, Z. Wang, M. G. Vergniory, C. Felser, R. J. Cava, and B. A. Bernevig, Beyond Dirac and Weyl fermions: Unconventional quasiparticles in conventional crystals, Science **353**, aaf5037 (2016).
[19] M. Udagawa and E. J. Bergholtz, Field-Selective Anomaly and Chiral Mode Reversal in Type-II Weyl Materials, Phys. Rev. Lett. **117**, 086401 (2016).
[20] D. Sabsovich, T. Meng, D. I. Pikulin, R. Queiroz, and R. Ilan, Pseudo field effects in type II Weyl semimetals: new probes for over titled cones, J. Phys. Condens. Matter **32**, 484002 (2020).
[21] S. Li, Z.-M. Yu, Y. Yao, and S. A. Yang, Type-II topological metals, Front. Phys. **15**, 43201 (2020).
[22] G. Chang, S. Y. Xu, D. S. Sanchez, S. M. Huang, C. C. Lee, T. R. Chang, G. Bian, H. Zheng, I. Belopolski, N. Alidoust,

H. T. Jeng, A. Bansil, H. Lin, and M. Z. Hasan, A strongly robust type II Weyl fermion semimetal state in Ta_3S_2, Sci. Adv. **2**, e1600295 (2016).

[23] K. Deng, G. Wan, P. Deng, K. Zhang, S. Ding, E. Wang, M. Yan, H. Huang, H. Zhang, Z. Xu, J. Denlinger, A. Fedorov, H. Yang, W. Duan, H. Yao, Y. Wu, S. Fan, H. Zhang, X. Chen, and S. Zhou, Experimental observation of topological Fermi arcs in type-II Weyl semimetal $MoTe_2$, Nat. Phys. **12**, 1105 (2016).

[24] L. Huang, T. M. McCormick, M. Ochi, Z. Zhao, M. T. Suzuki, R. Arita, Y. Wu, D. Mou, H. Cao, J. Yan, N. Trivedi, and A. Kaminski, Spectroscopic evidence for a type II Weyl semimetallic state in $MoTe_2$, Nat. Mater. **15**, 1155 (2016).

[25] J. Jiang, Z. K. Liu, Y. Sun, H. F. Yang, C. R. Rajamathi, Y. P. Qi, L. X. Yang, C. Chen, H. Peng, C. C. Hwang, S. Z. Sun, S. K. Mo, I. Vobornik, J. Fujii, S. S. Parkin, C. Felser, B. H. Yan, and Y. L. Chen, Signature of type-II Weyl semimetal phase in $MoTe_2$, Nat. Commun. **8**, 13973 (2017).

[26] Y. Y. Lv, X. Li, B. B. Zhang, W. Y. Deng, S. H. Yao, Y. B. Chen, J. Zhou, S. T. Zhang, M. H. Lu, L. Zhang, M. Tian, L. Sheng, and Y. F. Chen, Experimental Observation of Anisotropic Adler-Bell-Jackiw Anomaly in Type-II Weyl Semimetal $WTe_{1.98}$ Crystals at the Quasiclassical Regime, Phys. Rev. Lett. **118**, 096603 (2017).

[27] Y. Wang, E. Liu, H. Liu, Y. Pan, L. Zhang, J. Zeng, Y. Fu, M. Wang, K. Xu, Z. Huang, Z. Wang, H. Z. Lu, D. Xing, B. Wang, X. Wan, and F. Miao, Gate-tunable negative longitudinal magnetoresistance in the predicted type-II Weyl semimetal WTe_2, Nat. Commun. **7**, 13142 (2016).

[28] S. Y. Xu *et al.*, Discovery of Lorentz-violating type II Weyl fermions in LaAlGe, Sci. Adv. **3**, e1603266 (2017).

[29] P. Li, Y. Wen, X. He, Q. Zhang, C. Xia, Z. M. Yu, S. A. Yang, Z. Zhu, H. N. Alshareef, and X. X. Zhang, Evidence for topological type-II Weyl semimetal WTe_2, Nat. Commun. **8**, 2150 (2017).

[30] M. Y. Yao, N. Xu, Q. S. Wu, G. Autès, N. Kumar, V. N. Strocov, N. C. Plumb, M. Radovic, O. V. Yazyev, C. Felser, J. Mesot, and M. Shi, Observation of Weyl Nodes in Robust Type-II Weyl Semimetal WP_2, Phys. Rev. Lett. **122**, 176402 (2019).

[31] G. Ma, M. Xiao, and C. T. Chan, Topological phases in acoustic and mechanical systems, Nat. Rev. Phys. **1**, 281 (2019).

[32] H. Xue, Y. Yang, and B. Zhang, Topological acoustics, Nat. Rev. Mater. **7**, 974 (2022).

[33] F. Li, X. Huang, J. Lu *et al.*, Weyl points and Fermi arcs in a chiral phononic crystal, Nat. Phys. **14**, 30 (2017).

[34] V. Peri, M. Serra-Garcia, R. Ilan, and S. D. Huber, Axial-field-induced chiral channels in an acoustic Weyl system, Nat. Phys. **15**, 357 (2019).

[35] B. Zhang, Audible Landau levels, Nat. Phys. **15**, 307 (2019).

[36] X. Huang, W. Deng, F. Li, J. Lu, and Z. Liu, Ideal Type-II Weyl Phase and Topological Transition in Phononic Crystals, Phys. Rev. Lett. **124**, 206802 (2020).

[37] R. Ilan, A. G. Grushin, and D. I. Pikulin, Pseudo-electromagnetic fields in 3D topological semimetals, Nat. Rev. Phys. **2**, 29 (2019).

[38] See Supplemental Material at http://link.aps.org/supplemental/10.1103/PhysRevLett.130.266304 for effective Hamiltonians and antichiral zeroth LLs for the WPs based on kp perturbation theory (I), removing the surface dispersion (II), experimental discussions (III) and tight-binding model (IV).

[39] Z. M. Yu, Y. Yao, and S. A. Yang, Predicted Unusual Magnetoresponse in Type-II Weyl Semimetals, Phys. Rev. Lett. **117**, 077202 (2016).

[40] C. M. Wang, H.-P. Sun, H. Z. Lu, and X. C. Xie, 3D Quantum Hall Effect of Fermi Arcs in Topological Semimetals, Phys. Rev. Lett. **119**, 136806 (2017).

[41] C. Zhang, Y. Zhang, X. Yuan, S. Lu, J. Zhang, A. Narayan, Y. Liu, H. Zhang, Z. Ni, R. Liu, E. S. Choi, A. Suslov, S. Sanvito, L. Pi, H. Z. Lu, A. C. Potter, and F. Xiu, Quantum Hall effect based on Weyl orbits in Cd_3As_2, Nature (London) **565**, 331 (2018).